



Article

A Comprehensive Evaluation of Dual-Polarimetric Sentinel-1 SAR Data for Monitoring Key Phenological Stages of Winter Wheat

Mo Wang^{1,2} , Laigang Wang^{3,4,*}, Yan Guo^{3,4}, Yunpeng Cui^{1,2}, Juan Liu^{1,2}, Li Chen^{1,2}, Ting Wang^{1,2} and Huan Li^{1,2}

- ¹ Agricultural Information Institute, Chinese Academy of Agricultural Sciences, Beijing 100081, China; wangmo@caas.cn (M.W.); cuiyunpeng@caas.cn (Y.C.)
- ² Key Laboratory of Agricultural Big Data, Ministry of Agriculture and Rural Affairs, Beijing 100081, China
- ³ Institute of Agricultural Information Technology, Henan Academy of Agricultural Sciences, Zhengzhou 450002, China; guoyan@hnagri.org.cn
- ⁴ Key Laboratory of Huang-Huai-Hai Smart Agricultural Technology, Ministry of Agriculture and Rural Affairs, Zhengzhou 450002, China
- * Correspondence: wanglaigang@hnagri.org.cn

Abstract: Large-scale crop phenology monitoring is critical for agronomic planning and yield prediction applications. Synthetic Aperture Radar (SAR) remote sensing is well-suited for crop growth monitoring due to its nearly all-weather observation capability. Yet, the capability of the dual-polarimetric SAR data for wheat phenology estimation has not been thoroughly investigated. Here, we conducted a comprehensive evaluation of Sentinel-1 SAR polarimetric parameters' sensibilities on winter wheat's key phenophases while considering the incidence angle. We extracted 12 polarimetric parameters based on the covariance matrix and a dual-pol-version H- α decomposition. All parameters were evaluated by their temporal profile and feature importance score of Gini impurity with a decremental random forest classification process. A final wheat phenology classification model was built using the best indicator combination. The result shows that the Normalized Shannon Entropy (NSE), Degree of Linear Polarization (DoLP), and Stokes Parameter g2 were the three most important indicators, while the Span, Average Alpha ($\bar{\alpha}_2$), and Backscatter Coefficient σ_{VH}^0 were the three least important features in discriminating wheat phenology for all three incidence angle groups. The smaller-incidence angle (30–35°) SAR images are better suited for estimating wheat phenology. The combination of NSE, DoLP, and two Stokes Parameters (g2 and g0) constitutes the most effective indicator ensemble. For all eight key phenophases, the average Precision and Recall scores were above 0.8. This study highlighted the potential of dual-polarimetric SAR data for wheat phenology estimation. The feature importance evaluation results provide a reference for future phenology estimation studies using dual-polarimetric SAR data in choosing better-informed indicators.

Keywords: dual-polarimetric SAR; wheat phenology; Sentinel-1; polarimetric parameters



Citation: Wang, M.; Wang, L.; Guo, Y.; Cui, Y.; Liu, J.; Chen, L.; Wang, T.; Li, H. A Comprehensive Evaluation of Dual-Polarimetric Sentinel-1 SAR Data for Monitoring Key Phenological Stages of Winter Wheat. *Remote Sens.* **2024**, *16*, 1659. <https://doi.org/10.3390/rs16101659>

Academic Editors: Kevin Tansey, Lucio Mascolo, Mehdi Hosseini and Dipankar Mandal

Received: 4 March 2024

Revised: 25 April 2024

Accepted: 29 April 2024

Published: 8 May 2024



Copyright: © 2024 by the authors. Licensee MDPI, Basel, Switzerland. This article is an open access article distributed under the terms and conditions of the Creative Commons Attribution (CC BY) license (<https://creativecommons.org/licenses/by/4.0/>).

1. Introduction

Timely monitoring of crop phenology is essential for precision agriculture, as it crucially informs strategic planning and the implementation of agricultural practices such as irrigation, fertilization, and disease control. Certain phenological stages allow for optimizing irrigation and fertilizer schedules [1,2], while others exhibit higher susceptibility to pests and diseases [3]. Moreover, precise insight into crop phenology helps governmental agencies provide accurate crop productivity forecasts and make well-informed agricultural policy decisions. Wheat, as one of the most important crops worldwide, requires large-scale phenology observation for agronomic planning and decision making. Some agronomic measures are recommended according to phenological timing. For instance,

winter wheat's spring irrigation during regreening to heading is necessary to ensure the water requirements due to the deficiency in precipitation [4]. Post-flowering irrigation may elevate the risks of fungal diseases and lodging in wheat crops [5]. Under high-temperature conditions, it is recommended to implement limited irrigation during the flowering period to maximize yield [6].

Many attempts have been made for crop phenology monitoring, using satellite imageries either from optical or microwave sensors. Some indicators derived from optical remote sensing data are sensitive to crop growing stages, e.g., certain spectral bands, vegetation indices, and biophysical variables [7–9]. Some indicators derived from microwave radar images also demonstrated sensibility on crop phenology, e.g., backscattering coefficient, polarization ratio (VV/VH), and polarization parameters [10–12]. It is challenging to accomplish an ideal continuous phenology monitoring on the whole crop growing cycle solely using optical images due to interruption by unfavorable weather conditions (cloud cover, etc.). Microwave remote sensing is well-suited for crop growth monitoring due to its almost weather-independent observation capability with short time intervals [13].

SAR backscattering coefficients from different polarizations and their ratios were widely exploited to detect crop phenology, e.g., wheat, barley, and oil seed rape [14–16] using Sentinel-1 (S-1) data. One limitation of these studies is that only a few phenophases can be effectively detected with breakpoints of time series data. SAR backscattering coefficient data represent the overall strength of the returned radar signal that provides limited information about the surface characteristics of the target. Hence, they are often used along with optical images for crop phenology monitoring [12]. Polarimetric SAR (polSAR) data preserve information about polarization amplitude and the phase of the ground target, which are critical to identifying the backscattering mechanism and wave polarimetry. As crop growth progresses, there is not only an increase in backscatter but also a rise in the unpredictability of scattering, along with a more significant contribution of scattering from multiple/volume scattering [17]. Therefore, some polarimetric parameters that are related to backscattering mechanisms or wave polarimetry are potentially sensitive to crop phenology.

Several target decomposition approaches have been developed in the few past decades, including eigenvector- and eigenvalue-based and model-based decompositions [18]. Cloude-Pottier decomposition is an eigenvector- and eigenvalue-based decomposition method [19], which calculates the entropy (H), alpha angle (α), and anisotropy (A), subsequently partitioning the H- α plane into nine distinct zones relating to different scattering mechanisms. Fully polarimetric SAR data were proven effective by many studies to estimate crop phenology. For instance, RADARSAT-2 data were investigated for phenology retrieval of wheat and canola [17,20], rice [21], oat and barley [22], and multiple crops [23]; Uninhabited Aerial Vehicle Synthetic Aperture Radar (UAVSAR) data were used for canola, corn, and wheat [24] as well as a comparison between corn, sunflower, tomato, and permanent tree crops [25]. These crop phenology detection studies with polSAR data were based on several approaches. Some relied on coherence analysis across distinct polarimetric channels or phase differences between polarimetric channels [26–28] and some more studies directly utilized the parameters derived from various polarimetric decomposition algorithms [17,20,23,29]. In most cases, phenology retrieval was approached as a classification problem using indicators derived from polarimetric decomposition or other radar signal parameters. A tailored Cloude-Pottier decomposition for dual-polarization (dual-pol) SAR data was developed [30] and their ability to separate scattering mechanisms was assessed [31,32]. By testing on only dual-pol data of several full-pol SAR sensors, Ji and Wu [31] suggest that only HH-VV SAR can discriminate the three canonical scattering mechanisms; HH-HV or HV-VV cannot effectively differentiate scattering mechanisms, primarily stemming from the absence of co-polarization. While it is not possible to discriminate single scattering mechanisms using only dual-pol data with S-1's VV and VH polarization [27], extracted parameters such as Wave Entropy and average alpha can still be valuable indicators in crop monitoring applications [12,33,34]. Polarimetric parameters extracted from C-band S-1 data were

employed to retrieve phenophases of wheat and rapeseed [12], winter wheat and winter barley [35], and mustard and wheat [36]. Additionally, dual-pol X-band TerraSAR-X data featuring co-polarization combinations of HH and VV were utilized for monitoring rice phenology [37] and canola [38].

Among various SAR remote sensing data sources, S-1 data provide distinct advantages for crop monitoring regarding revisit frequency, image resolution, and free access. However, only a few parameters extracted from dual-pol S-1 data were evaluated and applied for crop phenology monitoring. The capability of dual-pol parameters has not been thoroughly investigated. Moreover, it is noted that the incidence angles of SAR images will impact microwave scatterings [22,31]. The effects of the incidence angle of SAR images against the phenology of vertically oriented crops, e.g., wheat, is still to be investigated. This study aims to (1) conduct a comprehensive evaluation of sensibilities of polarimetric parameters extracted from S-1 Single Look Complex (SLC) images on winter wheat's phenology while considering SAR images' incidence angle; (2) investigate the best feature combination for wheat phenology classification; and (3) build and evaluate a random forest classifier using the best feature combination for estimating winter wheat phenology.

2. Materials and Methods

2.1. Study Area

We focus on the Huang-Huai-Hai Plain, located in North China, as the study area. The Plain encompasses several critical wheat-growing provinces, yielding 80% of China's winter wheat production. In total, 167 of China's national Agricultural Meteorology Stations (AMS), which record meteorology data and crop phenology, are distributed in the Plain. Overall, 67 of the stations are dedicated to winter wheat observation. We selected 17 stations and their surrounding 1×1 km of square sub-sites as Areas of Interest (AOIs). The criteria for selecting those AMSs was more frequent phenology records that coincided with time series S-1 data coverage. Figure 1 illustrates the locations of the Huang-Huai-Hai Plain and the AOIs are indicated by the AMSs.

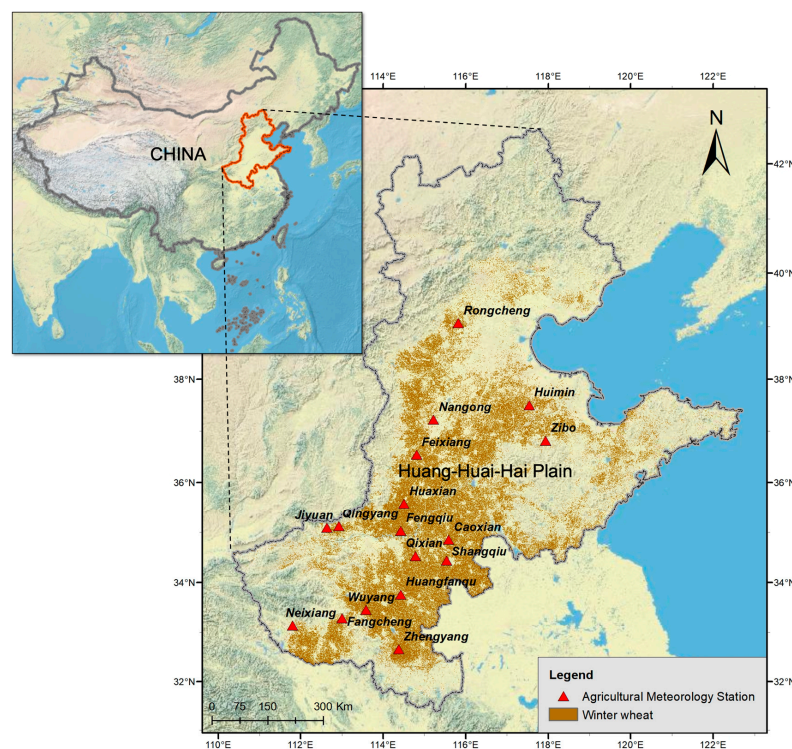


Figure 1. The location of the Huang-Huai-Hai Plain and the sub-sites of the study area are indicated by Agricultural Meteorology Stations. Winter wheat pixels of the 2017–2018 growing season from Dong, Wang, and Tian et al. [39] are shown in brown on the map.

2.2. Data

2.2.1. In Situ Wheat Phenology Observation and Wheat Map

In situ wheat phenology observation records from the 17 AMSs of our AOIs were acquired. Phenophases and observation dates were logged in a table. The records include 12 phenophases, i.e., emergence, three leaves, tillering, wintering period, regreening, standing, jointing, booting, heading, flowering, milk ripening, and maturity. We focus on phenophases of regreening and onwards that are critical for field management. Hence, eight phenophases' observations in 2018 after the regreening stage in each in situ record were selected (Table 1). The phenology observations were taken on crop fields of the AMS' closely adjacent area and are locally representative, according to the AMS phenology observation standard.

Table 1. Phenophases recorded by in situ wheat phenology observation and associated BBCH scale (from regreening onwards).

Phenophase	Description	BBCH Scale
Regreening	The wintering period ends and leaf turns green	25
Standing	Wheat plants transit from growing horizontally close to the ground to growing vertically upright	29
Jointing	Beginning of stem elongation	32
Booting	Flag leaf sheath extending	41
Heading	Tip of inflorescence emerged from the sheath, the first spikelet just visible	51
Flowering	Beginning of flowering: first anthers visible	61
Milk ripening	Watery ripe: first grains have reached half their final size	71
Maturity	Early dough	83

Additional phenology record attributes, including the AMS location and phenophase development percentage, were also retrieved for later use. The location coordinates of the AMSs were used to co-register the wheat fields. There was no fixed time interval on observation for each AMS. The observation time of the eight phenophases ranges from January to June. A total number of 98 phenology records were available for our AOIs. Phenophase development percentage is a crucial metric to determine phenophases in the BBCH code.

The winter wheat map provided by Dong, Wang, and Tian et al. [39] was used to identify wheat pixels within the AOIs (Figure 1). The map data are in 30-m resolution and has high accuracies based on assessment using survey samples.

2.2.2. Sentinel-1 SAR Imagery

We acquired the time series S-1 Single Look Complex (SLC) in Interferometric Wide swath (IW) mode for the 17 AOIs. The S-1 A/B constellation provides C-band dual-pol SAR data with a revisit time of approximately six days that is well-suited for time series agricultural monitoring.

The S-1 SLC images of the AOIs on targeted dates were downloaded from NASA's Earth Observing System Data and Information System (EOSDIS, <https://search.asf.alaska.edu/>). The SLC images are C-band SAR images with a dual-pol mode (VV+VH), capturing amplitude and phase information. The IW mode acquires data at 5 m by 20 m spatial resolution (single look). SLC images' acquisition dates did not entirely coincide with the AMS phenology observation dates. Therefore, the SLC images were selected based on the principle of "closest date" to avoid large time shifts between in situ phenology observation and selected SAR images. The date difference between the two observation sources was less than four days. SLC images of 98 dates were obtained, whose incidence angles range from 30.62 to 44.63 degrees.

2.3. Methods

The workflow of this study contains two major parts (Figure 2). First, several pre-processes are conducted to extract polarimetric parameters from the S-1 SLC images for the AOIs. The extracted parameters are then associated with the phenology records before splitting the dataset into training and test sets. We then conducted a wave polarimetry analysis echoing winter wheat's growing stages. Based on the wave polarimetry analysis, we applied an interactive process involving feature importance analysis and phenology classification modeling to find the best random forest (RF) classifier. Finally, we evaluated the model's performance in predicting winter wheat's phenological stages on a test set. Considering the range of SLC images' incidence angle, we carried out the feature importance analysis and modeling in three groups, i.e., the smaller-incidence-angle group (30–35°), medium-incidence-angle group (35–40°), and larger-incidence-angle group (40–45°).

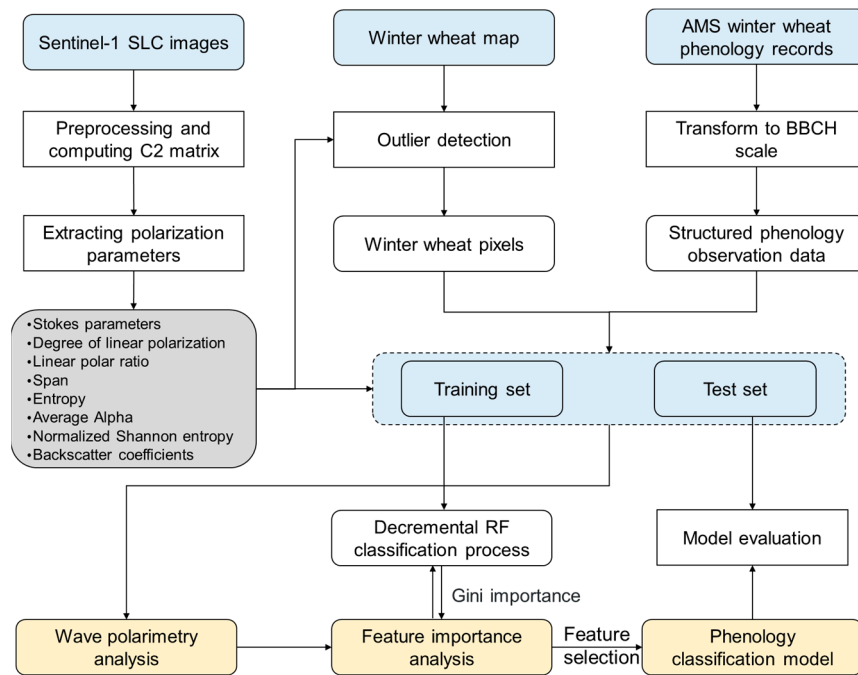


Figure 2. Workflow of the proposed method for evaluation of S-1's polarimetric parameters for winter wheat phenology monitoring.

2.3.1. SAR Data Processing and Polarimetric Decomposition

Polarimetric decomposition theories were initially developed for full-pol data and aimed to identify different microwave scattering mechanisms [33]. Based on the pioneering work of Cloude [30] and Cloude, et al. [40], we adopted their modified entropy/alpha decomposition method for dual-pol data to extract S-1's polarimetric parameters that are analogous to full-pol decomposition.

We extracted 12 SAR parameters from S-1 SLC images as listed in Table 2. The SAR parameters were derived from the 2×2 wave covariance matrix C_2 . Due to speckle, the C_2 matrix was generated from the S-1 vertical transmit (V) and dual-pol receive (V and H) data by means of spatial averaging, which is given by Equation (1).

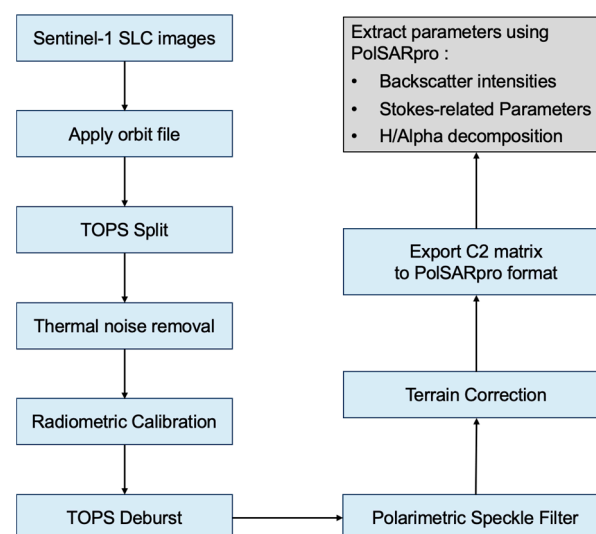
$$C_2 = \begin{bmatrix} C_{11} & C_{12} \\ C_{21} & C_{22} \end{bmatrix} = \begin{bmatrix} \langle |S_{VV}|^2 \rangle & \langle S_{VV}S_{VH}^* \rangle \\ \langle S_{VH}S_{VV}^* \rangle & \langle |S_{VH}|^2 \rangle \end{bmatrix} \quad (1)$$

where superscript * denotes the complex conjugate and $\langle \dots \rangle$ denotes the spatial average over a moving window. The Backscatter Coefficients for the VV and VH polarizations were obtained as the diagonal elements of the C_2 matrix.

Table 2. Parameters extracted from Sentinel-1 SLC images.

Indicators	Details	Equations
Stokes parameters	The partial polarization state of an electromagnetic (EM) wave (g_0, g_1, g_2, g_3)	See Equation (2)
Degree Of Linear Polarization (DoLP)	DoLP measures the proportion of linearly polarized components in the total signal received by the radar.	$DoLP = \frac{\sqrt{g_1^2 + g_2^2}}{g_0}$
Linear Polar Ratio (LPR)	The ratio of VV and VH intensities	$LPR = \frac{g_0 - g_1}{g_0 + g_1}$
Wave Entropy (H_2)	A measure of the uncertainty in the polarization of the received wave	See Equations (3)–(5)
Average Alpha ($\bar{\alpha}_2$)	Represents the angular separation, on the Poincaré sphere, between the polarization state of the transmitted wave and received wave	See Equations (3)–(5)
Normalized Shannon Entropy (NSE)	NSE characterizes the diversity or randomness of polarimetric backscattering. The sum of total backscatter power and the Barakat degree of polarization, normalized to between 0 and 1	See Equations (6) and (7)
Backscattering coefficient (σ^0)	Sigma naught VV and VH intensity. The measure of the radar return from a distributed target, defined as per unit area on the ground	
Span	The total intensity (VH + VV) received	

The two key data processing steps include preprocessing of SLC images to generate noise-free covariance matrix C_2 and extracting polarization parameters, as shown in Figure 3.

**Figure 3.** Flowchart of data processing steps for extracting S-1 polarimetric parameters. Steps in the blue background were implemented by SNAP and the grey background by PolSARpro.

Before generating the noise-free C_2 matrix, the SLC images underwent several calibration, correction, and noise removal procedures using the ESA SNAP tool with a processing graph. These preprocessing steps include applying the orbit file, TOPS Split, thermal noise removal, radiometric calibration, TOPS deburst, polarimetric speckle filter, and terrain correction, followed by exporting the C_2 matrix to the PolSARpro format. Figure 3 illustrates the complete data processing flow. It should be noted that thermal noise removal is an indispensable step for applying dual-pol S-1 SLC data. Simply applying SNAP's ThermalNoiseRemoval without correcting for the off-diagonal entries of noisy C_2 would be erroneous. We applied the thermal noise removal proposed by Mascolo et al. [41]. This method exploits SNAP's ThermalNoiseRemoval module to remove thermal noise from the C_2 matrix and it can be implemented with SNAP's processing graph.

The following step was extracting SAR parameters with the PolSARpro tool. Extracted parameters (Table 2) include six Stokes-related parameters (four Stokes Parameters, Degree of Linear Polarization, and Linear Polar Ratio), three polarimetric decomposition parameters (Wave Entropy, Average Alpha, and Normalized Shannon Entropy), and three backscatter intensity indicators (VV and VH backscattering coefficient, Span). All processed images are exported in 10 m pixel spacing and clipped to AOIs for later analysis.

(1) Stokes Parameters

Stokes Parameters describe the scattering from a partially polarized EM field that contains all the polarimetric information. The four Stokes Parameters are defined as follows:

$$\begin{bmatrix} g_0 \\ g_1 \\ g_2 \\ g_3 \end{bmatrix} = \begin{bmatrix} |E_H|^2 + |E_V|^2 \\ |E_H|^2 - |E_V|^2 \\ 2|E_H||E_V|\cos \phi_{HV} \\ 2|E_H||E_V|\sin \phi_{HV} \end{bmatrix} = \begin{bmatrix} C_{11} + C_{22} \\ C_{11} - C_{22} \\ 2R_e(C_{12}) \\ 2I_m(C_{12}) \end{bmatrix} \quad (2)$$

where $|E|$ is the amplitude of the EM wave and ϕ_{HV} is the phase difference between H and V. R_e and I_m denote the real part and imaginary part of the complex number, respectively. The first Stokes Parameter (g_0) indicates the total intensity of the radar backscatter (polarized and unpolarized), which is the sum of the powers of the two orthogonally polarized received waves. The other three parameters (g_1 , g_2 , and g_3) describe the properties of the polarized portion of the electromagnetic field.

Based on the four Stokes Parameters, several supplementary parameters that characterize the condition of the scattered EM field can be derived, including the Degree Of Linear Polarization (DoLP) and the linear polarization ratio (LPR).

(2) H- α decomposition for dual-polarimetric SAR data

We adopted the dual-pol version of entropy/alpha decomposition [30] to derive Wave Entropy (H_2) and Average Alpha ($\bar{\alpha}_2$). In the dual-pol case, the physical interpretation of H_2 and $\bar{\alpha}_2$ are different from that of entropy and alpha of the full-pol case. H_2 describes the uncertainty in the polarization of the received wave. $\bar{\alpha}_2$ is the average angular separation between the polarization state of the transmitted wave and the received one.

For S-1 dual-pol data (VV and VH modes), the following forms of the 2×2 wave coherency matrix $[J_V]$ are estimated via local averaging:

$$[J_V] = \begin{bmatrix} \langle S_{VV}S_{VV}^* \rangle & \langle S_{VV}S_{VH}^* \rangle \\ \langle S_{VH}S_{VV}^* \rangle & \langle S_{VH}S_{VH}^* \rangle \end{bmatrix} \quad (3)$$

Based on the interpretation of normalized eigenvalues as probabilities P_i and considering 2×2 coherency matrix problems according to Cloude [30], we can derive the second

eigenvector entirely from the principal vector using orthogonality. The entropy/alpha parameterization of the wave coherency matrix $[J]$ is obtained with Equation (4).

$$[J] = \begin{bmatrix} J_{xx} & J_{xy} \\ J_{xy}^* & J_{yy} \end{bmatrix} \Rightarrow \begin{cases} [U_2] = \begin{bmatrix} \cos \alpha & -\sin \alpha e^{-i\delta} \\ \sin \alpha e^{i\delta} & \cos \alpha \end{bmatrix} \\ [D] = (\lambda_1 + \lambda_2) \begin{bmatrix} P_1 & 0 \\ 0 & P_2 \end{bmatrix} \\ \bar{\alpha}_2 = P_1 \alpha + P_2 \left(\frac{\pi}{2} - \alpha\right) = \alpha(P_1 - P_2) + P_2 \frac{\pi}{2} \\ H_2 = \sum_{i=1}^2 P_i \log_2 P_i \end{cases} \quad (4)$$

$$\alpha = \cos^{-1}(|e_1|) \quad 0 \leq \alpha \leq 90^\circ \quad (5)$$

where P_i denotes probabilities of the statistically independent polarized states by normalizing the eigenvalues to the unit sum of λ_1 and λ_2 . α denotes the scattering mechanism selected for the principal eigenvector e_1 .

(3) Normalized Shannon Entropy

Normalized Shannon Entropy (NSE) is a parameter to characterize the diversity or randomness of polarimetric backscattering. It is based on the concept of Shannon Entropy, which measures the uncertainty or information content in a random variable.

The normalized Shannon Entropy (NSE) is computed as follows:

$$\text{NSE} = \frac{SE}{SE_{\max}} \quad (6)$$

$$SE = \log(\pi^2 e^2 |C_2|) \quad (7)$$

where SE is the Shannon Entropy and H_{\max} is the maximum Shannon Entropy, which occurs when the energy is uniformly distributed among all polarization states. C_2 is the 2×2 covariance matrix extracted from the scattering matrix S . The NSE ranges from 0 to 1, where 0 indicates a fully polarized scenario and 1 indicates complete depolarization or randomness.

2.3.2. Outlier Detection on Wheat Cropping Pixels

To minimize noise data in wheat pixels, we carried out an outlier detection procedure using the Isolation Forest outlier detection model with derived polarimetric SAR parameters. The Isolation Forest model employs a tree-based approach to isolate anomalies efficiently by randomly selecting features and constructing isolation trees, enabling the identification of outliers as instances that require fewer splits to be isolated within the tree structure. We refer to Dong, Fu, and Wang et al. [39] for mathematical details of the model. The number of base estimators was set to 100. Outlying pixels were removed through the Isolation Forest filtering process as misclassified wheat pixels by fitting and running the model on each AOI.

2.3.3. Feature Importance Evaluation and Decremental Classification of Phenophase

We designed an iterative process to decide the importance of indicators and find the best feature combination for phenology classification interactively based on the random forest classifier (see Figure 4). First, samples were split into 85% training and 15% testing sets for each incidence angle group. With the training set, we adopted a five-fold cross-validation strategy to train random forest classifiers using Gini impurity as a criterion for the tree-building process. The random forest classifier was set to a default parameterization (trees = 100). The mean Kappa for the five folds was calculated as the model performance metric. For each training fold, feature importance was evaluated by sorting their Gini importance score. The importance ranking for each feature was determined by the five-fold average Gini importance values. The feature that ranks as least important was then omitted.

The above five-fold cross-validation process was repeated with the remaining indicators until the last feature was left. The most important indicators for winter wheat phenophase classification were hereby determined as those leading to the highest mean validating Kappa score. We define this modeling process as a decremental classification.

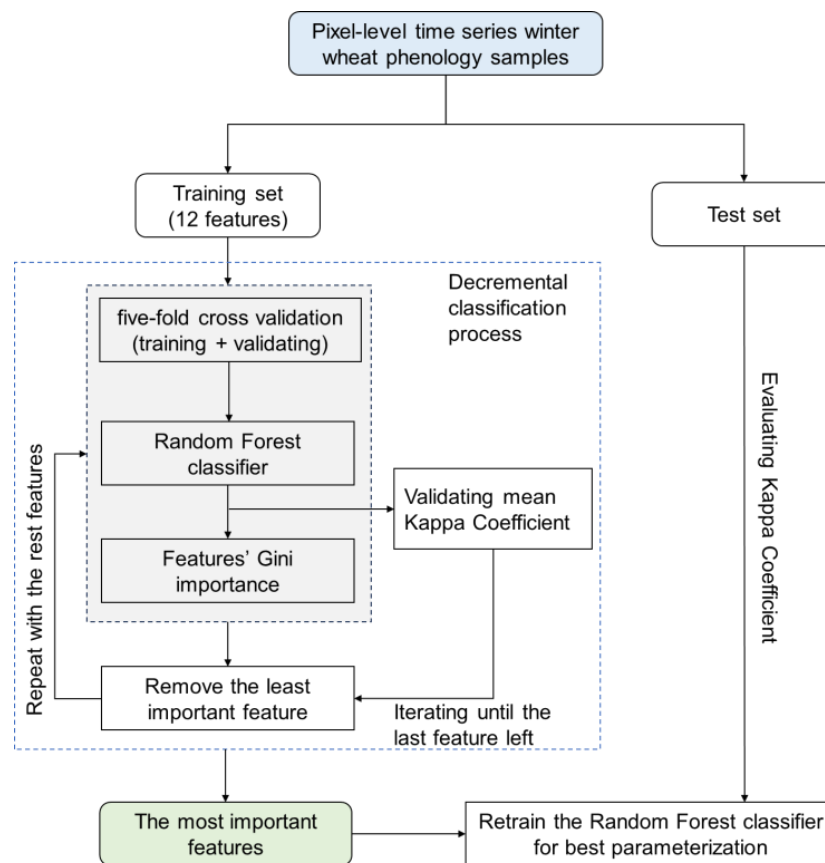


Figure 4. The decremental classification process of important feature selection with a random forest classifier.

With the most important indicators, we retrained the random forest classifier with different model parameter combinations to find the best parameterization using a 5-fold cross-validating strategy. Model performance was finally evaluated with the test set.

3. Results

3.1. Backscattered Wave Polarimetry Analysis

We aggregated each AOI's pixel-wise polarimetric parameters by averaging them to form an AOI-level sample set containing mean polarimetric parameter values and phenophase records. Phenology records were plotted to examine how polarimetric parameters change against phenology development (Figures 5–7). It can be observed that most parameters, including H_2 , $\bar{\alpha}_2$, LPR, NSE, DoLP, Span, σ_{VV}^0 , g_0 , g_1 , and g_2 , show evident sensitivity to wheat phenophase. The underlying explanation contributes to the fact that biomass accumulates and the canopy structure and water content change as the crop matures. As a result, the polarimetry of the received wave varies as phenophase progresses.

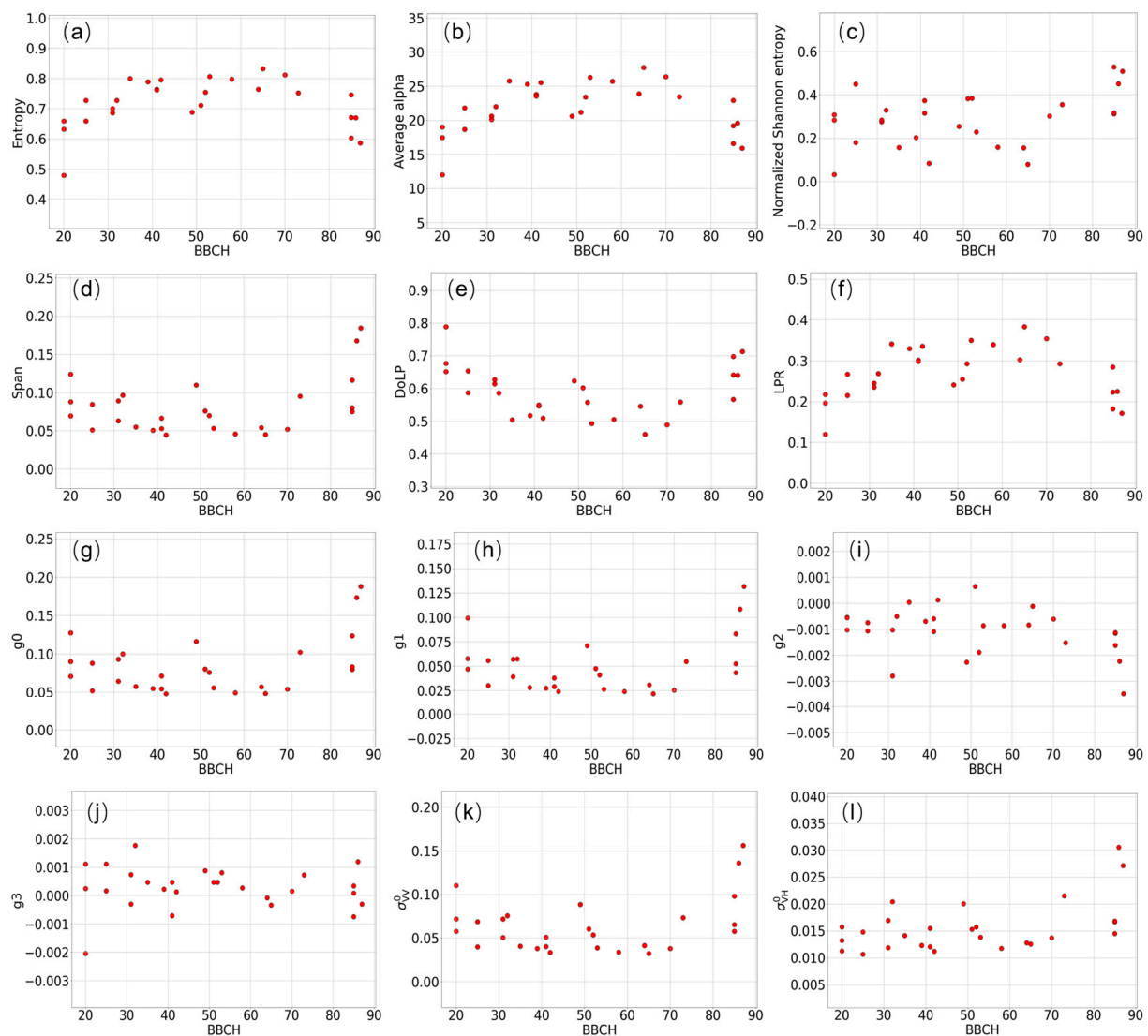


Figure 5. Scatter plots of polarimetric parameters against winter wheat phenophase in the BBCH scale for the smaller-incidence-angle group ($30\text{--}35^\circ$). Subfigures are BBCH against H_2 (a), $\bar{\alpha}_2$ (b), Normalized Shannon Entropy (c), Span (d), DoLP (e), LPR (f), g_0 (g), g_1 (h), g_2 (i), g_3 (j), σ_{VV}^0 (k), and σ_{VH}^0 (l), respectively.

Before the greening stage, the wheat canopy was in its initial seedling state. The SAR response was dominated by bare soil. From the greening stage to the standing stage (BBCH 25–30), the wheat canopy starts to develop again while plant height is low. Bare soil between crop rows leads to the majority contribution of soil to the SAR response. Surface scattering dominates during these stages. H_2 and $\bar{\alpha}_2$ were relatively low ((a) and (b) in Figures 5–7). Backscatter energy σ_{VV}^0 ((m) in Figures 5–7) began to decrease from the greening to the standing stage due to vertical development of the wheat plant. So did the DoLP ((e) in Figures 5–7), Span ((d) in Figures 5–7), g_0 ((g) in Figures 5–7), and g_1 ((h) in Figures 5–7). On the other hand, LPR ((f) in Figures 5–7) increases during this stage.

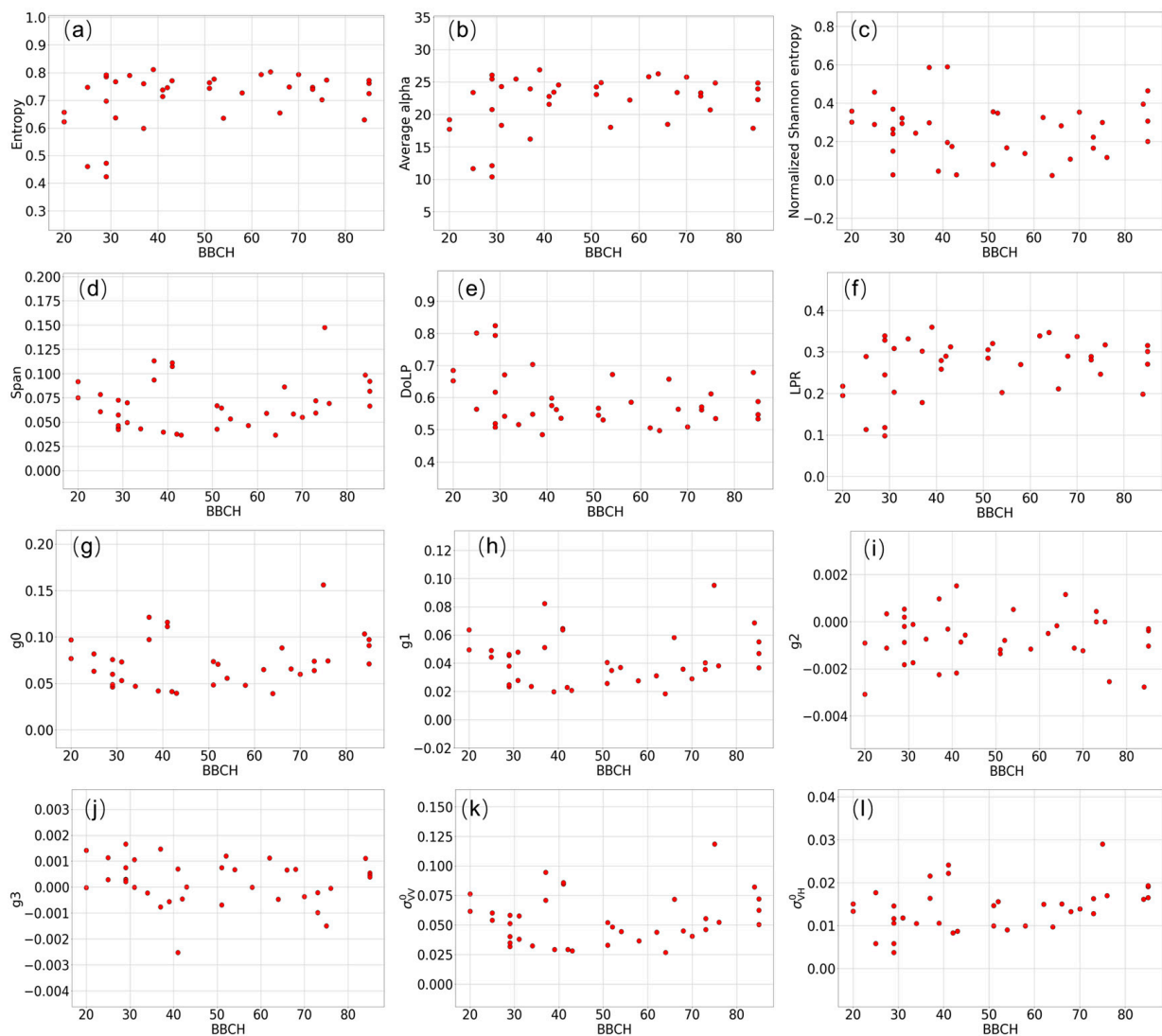


Figure 6. Scatter plots of polarimetric parameters against winter wheat phenophase in the BBCH scale for the median-incidence-angle group (35–40°). Subfigures are BBCH against H_2 (a), $\bar{\alpha}_2$ (b), Normalized Shannon Entropy (c), Span (d), DoLP (e), LPR (f), g_0 (g), g_1 (h), g_2 (i), g_3 (j), σ_{VV}^0 (k), and σ_{VH}^0 (l), respectively.

During jointing (BBCH 30–39) and booting (BBCH 41–49), crop stems begin to develop and leaves grow longer and thicker. Meanwhile, flag leaves develop rapidly, crop height grows, and canopy coverage reaches maximum. As plant growth progresses, the soil’s contribution to surface scattering diminishes while volume scattering by plants becomes more prominent. Additionally, the radar signal’s complexity grows due to the enhanced depolarization caused by the vegetation. This depolarization stems from the multiple-point scatterers, in contrast to a single equivalent point scatterer [42,43]. As a result, H_2 and $\bar{\alpha}_2$ values reached maximum values of around 0.8–0.85 and approximately 28° in the booting stage, respectively, as shown in (a) and (b) in Figures 5–7. The σ_{VV}^0 continued the decrease in the jointing and booting stages. The decrease is mainly due to the vegetation attenuation effect, caused by the vertical elongation development of stems and leaves in these phases, which leads to attenuation in radar backscatter. Although the vegetation scattering and attenuation effects are coupled, the impact of vegetation attenuation on the soil contribution is more significant for narrow-leaf crops like wheat during its early phenological stages [23,44]. σ_{VV}^0 , DoLP, Span, g_0 , and g_1 continued decreasing. LPR reached its peak and then started declining during jointing and booting.

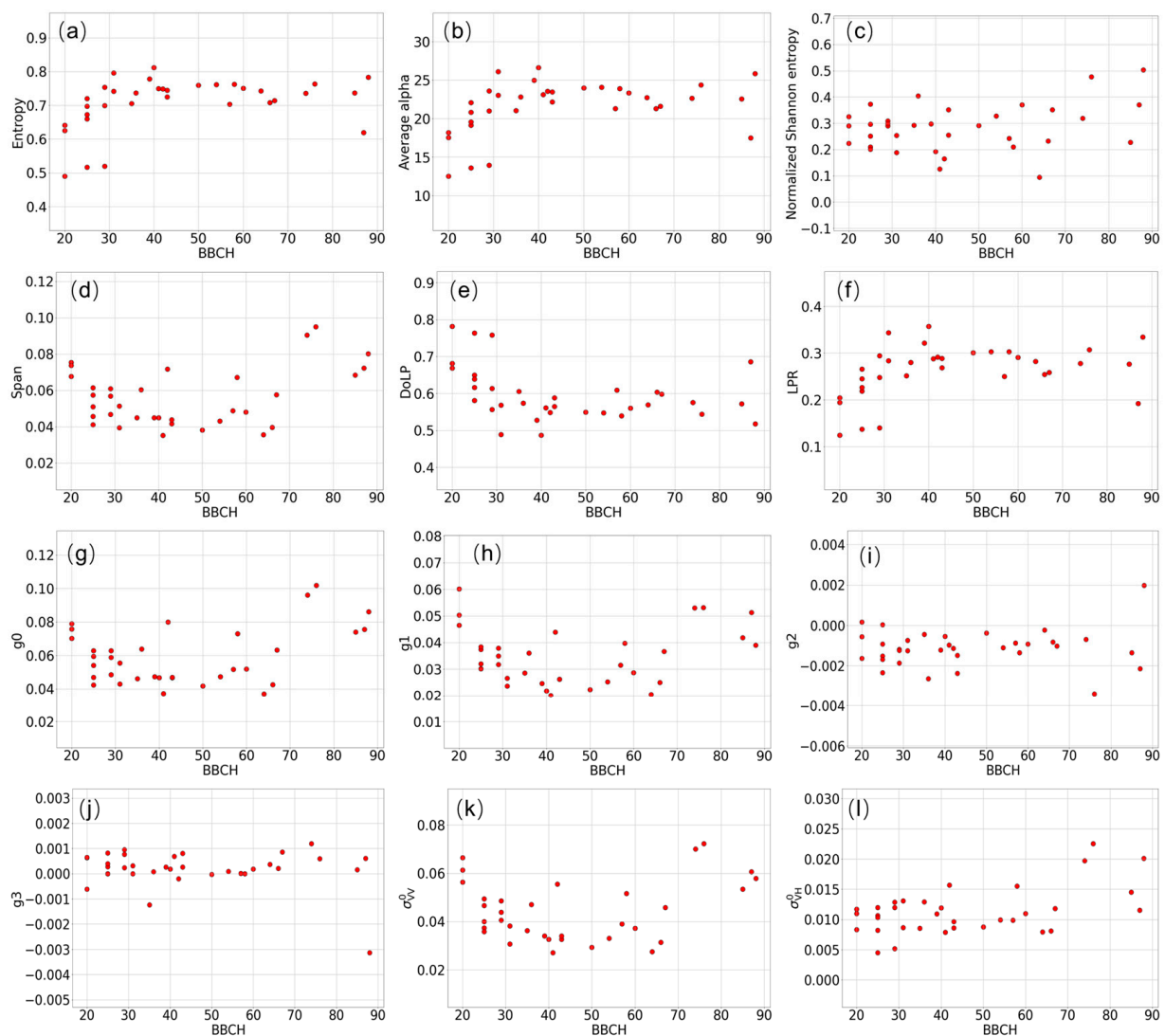


Figure 7. Scatter plots of polarimetric parameters against winter wheat phenophase in the BBCH scale for the larger-incidence-angle group (40–45°). Subfigures are BBCH against H_2 (a), $\bar{\alpha}_2$ (b), Normalized Shannon Entropy (c), Span (d), DoLP (e), LPR (f), g_0 (g), g_1 (h), g_2 (i), g_3 (j), σ_{VV}^0 (k), and σ_{VH}^0 (l), respectively.

During the heading stage (BBCH 50–60), the wheat spike (ear) began to emerge from the leaf sheath of the flag leaf after the uppermost leaf swelled into a flag, enclosing the spike within it. At this stage, biomass, Leaf Area Index (LAI), and plant height commonly reach their maximum values, leading to a more diverse appearance of the entire field, notably impacting the SAR signal [15]. Meanwhile, the vegetation attenuation effect reaches its maximum, leading to radar backscatter σ_{VV}^0 at its lowest level. Then, the radar backscatter rises with increasing biomass, given that the dominant factor is the vegetation scattering effect rather than the attenuation effect. H_2 and $\bar{\alpha}_2$ values during and after the heading stage experienced a decline. This indicates the ongoing desiccation of the plants and an increased soil contribution to the signal. Surface scattering of the soil regained significance, while the proportion of volume scattering from vegetation declined, as evidenced by decreasing alpha values. DoLP, g_0 , and g_1 started increasing in the heading stage. LPR showed litter variation in this stage.

Flowering (BBCH 61–70) and the milk ripening stage (BBCH 71–87) are vital phases for fruit development. The plant exhibits consistent or slightly decreasing biomass and height values at the flowering stage. The water content of the entire plant and the grains begins to

fall, followed by a significant reduction in vegetation water content in the ripening stage. The leaf color transitioned from green to yellow. During this period, LAI decreases and the soil likely has a growing impact on the radar signal once again [35]. During flowing and milk ripening, σ_{VV}^0 increased from around 0.05 to 0.15. LPR, Span, g_0 , and g_1 decreased to a local minimum and then increased sharply during the flowering and ripening stages. Meanwhile, DoLP showed a reverse pattern.

At the Mature and Senescence Stages (BBCH 88–100), LAI, biomass, and plant water content decrease dramatically, resulting in smaller crop coverage. The soil likely has a growing impact on the radar signal once again. The vegetation scattering effect is weakened. Hence, the σ_{VV}^0 decreases. The depolarization of the wave by vegetation was further attenuated due to the decreasing biomass, resulting in declining H_2 values. Also, the wave polarimetry change can be linked to changes in vegetation water content during maturity and senescence. An increase in crop absorption of wave energy occurred during wet vegetation conditions and a decrease in drying conditions [45].

3.2. SAR Parameters' Sensitivity to Phenological Stages

The feature importance of the 12 SAR parameters was recursively updated for the selection of the most important indicators for the three incidence angle groups. Figure 8 illustrates the cross-validating performance of the phenophase classification by Kappa score against the number of indicators. Four indicators were identified as the best feature combinations for phenophase classification for all three incidence angle groups. NSE, DoLP, and g_2 were among the most important indicators for all three incidence angle groups. For the smaller-incidence-angle group and larger-incidence-angle group, the four most important indicators were NSE, DoLP, g_2 , and g_0 in descending order of importance and NSE, DoLP, g_2 , and Wave Entropy for the medium-incidence-angle group. SAR parameters derived from smaller-incidence-angle images were generally more sensitive to phenological development, as evidenced by a larger Kappa score curve in Figure 8. As for the least important features, we observed that Span, $\bar{\alpha}_2$, and σ_{VH}^0 were the three least important features to discriminate wheat phenology for all incidence angle groups.

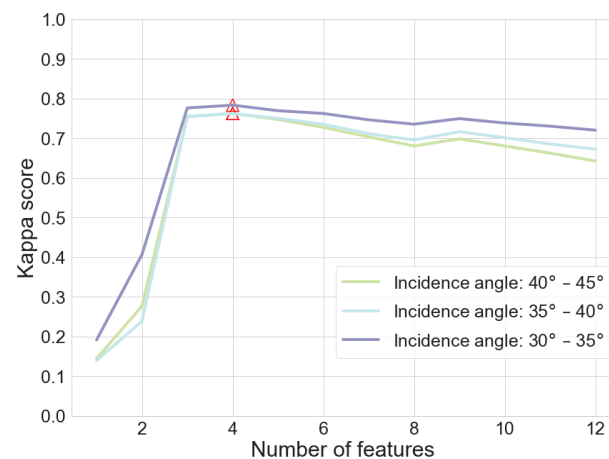


Figure 8. Mean Kappa score of cross-validations with different feature numbers for datasets of three incidence angle groups. Red triangles denote the points of the highest Kappa score.

3.3. Phenophase Classification Models

The best model parameters were determined for each incidence angle group using a cross-validated grid-search strategy. The best parameters were set to that minimal sample leaf equals 1, minimal sample split equals 2, number of trees equals 200, and Gini impurity as the classification criterion. Table 3 lists model evaluation metrics for the three incidence angle groups. In general, the classification model with smaller-incident-angle images had the highest performance in terms of weighted average precision (0.835), weighted average recall (0.834), and Kappa (0.799), followed by the larger-incident-angle group (Kappa 0.785)

and the median-incidence-angle group (Kappa 0.783) with similar performance. The performance disparities among the three models are not distinctly evident.

Table 3. Model performance of the random forest phenophase classification models.

Random Forest Classifier Models	Performance Metrics		
	Weighted Average Precision	Weighted Average Recall	Kappa
Smaller incidence angle (30–35°)	0.835	0.834	0.799
Medium incidence angle (35–40°)	0.811	0.812	0.783
Larger incidence angle (40–45°)	0.815	0.815	0.785

Figure 9 compares the phenophase identification capability (F1 score) of the three classification models concerning each phenophase. The classification model with smaller-incident-angle images outperforms the other two for most phenophases, except for jointing, booting, and milk ripening. For the smaller-incident-angle group, the model exhibited the highest F1 scores for regreening (0.81), standing (0.85), heading (0.81), following (0.83), and maturity (0.94) stages. Meanwhile, the phenophases with the highest F1 score for the medium-incidence-angle group were jointing (0.85) and booting (0.86). In comparison, the milk ripening stage witnessed the highest F1 score for the higher-incidence-angle group.

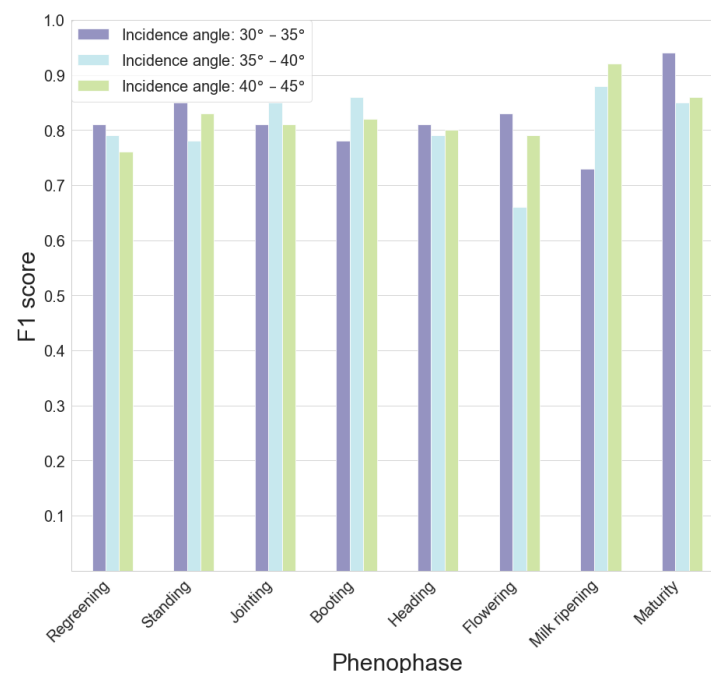


Figure 9. F1 score of each phenophase on the test set for the three incidence angle groups.

4. Discussion

4.1. Wave Polarimetry

SAR scattering mechanisms for full-pol SAR data at different phenophases of many crops, including wheat, have been extensively discussed [15,23,42,43,46]. The scattering mechanisms of full-pol SAR at different phenophases were determined as the crop developed. However, how the parameters extracted from dual-pol SAR data reflect wheat growing stages remains to be thoroughly investigated. We elaborated temporal profiles of the 12 indicators extracted from the dual-pol H- α decomposition and Stokes Parameters. The wave polarimetry analysis reveals that regardless of the incidence angle, H_2 , $\bar{\alpha}_2$, NSE, LPR, DoLP, Span, σ_{VV}^0 , g_0 , g_1 , and g_2 showed evident sensitivity to key wheat phenophases.

The interpretation of polarimetric features in relation to a target can pose challenges. For vertically oriented crops like wheat, most ambient waves, and those that undergo scattering within a distributed target like a crop canopy are typically only partially polarized. Firstly, the backscatter intensities of different polarization and their ratio were essential indicators as crop canopy develops. As the crop canopy develops a more complex structure, multiple scattering events lead to unequal phase and intensity of the horizontal (H) and vertical (V) components of the EM wave. Consequently, σ_{VV}^0 , σ_{VH}^0 , and LPR are theoretically correlated with phenology progress. However, in the early growing stages, bare soil between crop rows leads to the majority contribution of soil to the SAR response while plant height is low. Consequently, cross-polarized scattering kept low; hence, σ_{VH}^0 was significantly lower than σ_{VV}^0 and relatively constant from BBCH 20–40. σ_{VV}^0 was a better phenology indicator than σ_{VH}^0 . Meanwhile, Stokes components and their related parameters (DoLP and Span) were also affected by this underlying cause.

Shannon Entropy (SE) is a measure that is composed of two elements that are associated with the total backscatter power and the degree of polarization. SE incorporates a component of total power. It is possible that early in the season, the soil's contributions, particularly due to soil moisture, might be affecting SE. Once the canopy forms, SE was closely related to crop structure and water content as a strong indicator of phenology from BBCH 40–90.

It should be noted that some of the parameters were correlated and should be distinguished for future phenology classification tasks. The temporal profiles of the extracted parameters reveal that H_2 and $\bar{\alpha}_2$, Span and g_0 , and DoLP and g_1 are positively correlated, respectively. LPR was negatively correlated with DoLP. The redundant features could lead to unnecessary computational costs and higher overfitting risk for classification or regression tasks. This justifies the need for feature importance evaluation and feature selection procedures prior to phenology classification modeling.

4.2. Feature Importance

Feature importance analysis showed that NSE, DoLP, and g_2 are the three most important indicators for all three incidence angle groups. This conclusion provides a reference for selecting indicators in building wheat phenology classifiers using dual-pol SAR data. However, we should note that the feature importance evaluation was based on the Gini impurity in fitting a random forest classifier. The feature importance result does not denote an absolute importance for estimating wheat phenology. Other indicators, e.g., H_2 , $\bar{\alpha}_2$, σ_{VV}^0 , and Span, also showed variations against phenology development. The temporal profile of σ_{VV}^0 showed a prominent variance as wheat growth advanced. Other studies also suggested that S-1's Backscatter Coefficients can be related to wheat phenology. For example, Nasrallah, Baghdadi, and El Hajj et al. [16] claimed that σ_{VV}^0 and σ_{VH}^0 and their ratio can estimate certain wheat phenophase at certain incidence angle levels based on local extrema and breakpoints. Other studies also verified that σ_{VV}^0 is sensitive to vegetation wetness and peaks at the wheat stem elongation stage [47]. However, σ_{VV}^0 , σ_{VH}^0 , and their ratio failed to estimate the phenophases of the whole growing circle. In our case, σ_{VV}^0 was not included in the best feature set for phenology classification. Its importance ranks were 6th, 10th, and 9th for smaller, medium, and larger incidence angles, respectively. The underlying reason is that σ_{VV}^0 fluctuates more frequently compared to Entropy and Stokes Parameters during the whole growth circle. Therefore, σ_{VV}^0 is not an ideal feature in forming a rational criterion for the decision trees in the classifier. It should be noted that our model did not involve temporal indicators and could not learn indicators' fluctuation patterns. If combined with temporal information, e.g., DOY (day of the year) or accumulated temperature, indicators like LPR, DoLP, and σ_{VV}^0 could be significant for estimating wheat phenology.

4.3. Phenology Classification Results

Model evaluation with a test set shows that the SAR images of smaller incidence angles are better suited for estimating wheat phenology. The model with smaller-incidence-angle data achieved a better-estimating precision for all phenophases. The standing, following, and maturity stages witnessed the highest predicting score. This could be related to the indicators NSE, DoLP, g2, and g0, which were at their local extremes in those stages.

The reason that smaller-incidence-angle images outperformed the other two groups is related to the backscatter response, shadowing, and canopy structure of the crop. The SAR backscatter response from vegetation varies with the incidence angle. At smaller incidence angles, more energy penetrates the canopy, resulting in stronger backscatter signals. At larger angles, the radar signal interacts more with the top layers of vegetation, which may lead to more complex scattering behavior due to multiple scattering effects. At larger incidence angles, vegetation can cast shadows on the ground, affecting the radar signal received by the sensor. This can result in areas of reduced backscatter intensity or signal attenuation, particularly in dense vegetation. Different vegetation types and canopy structures respond differently to changes in incidence angle. Some vegetation types may exhibit stronger backscatter signals at certain angles due to their canopy structure and orientation relative to the radar beam [48,49]. In our case, smaller incidence angles provide better penetration into the vertically oriented wheat canopy and result in stronger backscatter signals, particularly for middle and late phenology stages featured by dense vegetation.

5. Conclusions

This study evaluated 12 parameters extracted from dual-pol S-1 data for wheat phenology classification while considering incidence angles of image acquisition. Feature importance evaluation and phenology classification results showed that

- NSE, DoLP, and g2 are the three most important indicators for all three incidence angle groups. The three indicators of least importance for all three groups were Span, $\bar{\alpha}_2$, and σ_{VH}^0 ;
- For the smaller-incidence-angle group (30°–35°) and larger-incidence-angle group (40°–45°), the four most important indicators were NSE, g0, H_2 , and g1 in descending order of importance. The four most important indicators for the medium-incidence-angle group were NSE, DoLP, g2, and H_2 ;
- Dual-pol SAR indicators are capable of estimating wheat phenology at a good precision. For all eight key phenophases, the average Precision and Recall were both above 0.8;
- Classification models trained on smaller-incidence-angle SAR images had better performance. The smaller-incidence-angle SAR images are better suited for estimating wheat phenology.

Overall, this study highlighted the potential of dual-pol SAR data for wheat phenology estimation. The results provide a reference for other phenology estimation studies using dual-pol SAR data in choosing better-informed indicators.

Author Contributions: Conceptualization, M.W. and L.W.; methodology, M.W.; validation, Y.G., Y.C. and L.C.; investigation, M.W.; resources, J.L.; data curation, T.W.; writing—original draft preparation, M.W.; writing—review and editing, L.W.; visualization, M.W. and H.L. All authors have read and agreed to the published version of the manuscript.

Funding: This research was funded by the Open Research Fund of Key Laboratory of Huang-Huai-Hai Smart Agricultural Technology, Ministry of Agriculture and Rural Affairs, grant number 202304; National Key R&D Program of China project, grant number 2023YFD1600305.

Data Availability Statement: Wheat map data are publicly provided by Dong, Fu, and Wang et al. via an open-data repository (<https://doi.org/10.6084/m9.figshare.12003990>).

Conflicts of Interest: The authors declare no conflicts of interest.

References

- Bouchet, A.-S.; Laperche, A.; Bissuel-Belaygue, C.; Snowdon, R.; Nesi, N.; Stahl, A. Nitrogen use efficiency in rapeseed. A review. *Agron. Sustain. Dev.* **2016**, *36*, 38. [[CrossRef](#)]
- Sakamoto, T.; Yokozawa, M.; Toritani, H.; Shibayama, M.; Ishitsuka, N.; Ohno, H. A crop phenology detection method using time-series MODIS data. *Remote Sens. Environ.* **2005**, *96*, 366–374. [[CrossRef](#)]
- Vreugdenhil, M.; Wagner, W.; Bauer-Marschallinger, B.; Pfeil, I.; Teubner, I.; Rüdiger, C.; Strauss, P. Sensitivity of Sentinel-1 backscatter to vegetation dynamics: An Austrian case study. *Remote Sens.* **2018**, *10*, 1396. [[CrossRef](#)]
- Kahil, M.T.; Connor, J.D.; Albiac, J. Efficient water management policies for irrigation adaptation to climate change in Southern Europe. *Ecol. Econ.* **2015**, *120*, 226–233. [[CrossRef](#)]
- Wegulo, S.N.; Baenziger, P.S.; Nopsa, J.H.; Bockus, W.W.; Hallen-Adams, H. Management of Fusarium head blight of wheat and barley. *Crop Prot.* **2015**, *73*, 100–107. [[CrossRef](#)]
- Wang, Y.; Zhang, X.; Liu, X.; Zhang, X.; Shao, L.; Sun, H.; Chen, S. The effects of nitrogen supply and water regime on instantaneous WUE, time-integrated WUE and carbon isotope discrimination in winter wheat. *Field Crops Res.* **2013**, *144*, 236–244. [[CrossRef](#)]
- Pan, Z.; Huang, J.; Zhou, Q.; Wang, L.; Cheng, Y.; Zhang, H.; Blackburn, G.A.; Yan, J.; Liu, J. Mapping crop phenology using NDVI time-series derived from HJ-1 A/B data. *Int. J. Appl. Earth Obs. Geoinf.* **2015**, *34*, 188–197. [[CrossRef](#)]
- Mulla, D.J. Twenty five years of remote sensing in precision agriculture: Key advances and remaining knowledge gaps. *Biosyst. Eng.* **2013**, *114*, 358–371. [[CrossRef](#)]
- Verbesselt, J.; Hyndman, R.; Zeileis, A.; Culvenor, D. Phenological change detection while accounting for abrupt and gradual trends in satellite image time series. *Remote Sens. Environ.* **2010**, *114*, 2970–2980. [[CrossRef](#)]
- Betbeder, J.; Fieuzal, R.; Philippets, Y.; Ferro-Famil, L.; Baup, F. Contribution of multitemporal polarimetric synthetic aperture radar data for monitoring winter wheat and rapeseed crops. *J. Appl. Remote Sens.* **2016**, *10*, 026020. [[CrossRef](#)]
- Phung, H.-P.; Lam-Dao, N.; Nguyen-Huy, T.; Le-Toan, T.; Apan, A.A. Monitoring rice growth status in the Mekong Delta, Vietnam using multitemporal Sentinel-1 data. *J. Appl. Remote Sens.* **2020**, *14*, 014518. [[CrossRef](#)]
- Mercier, A.; Betbeder, J.; Baudry, J.; Le Roux, V.; Spicher, F.; Lacoux, J.; Roger, D.; Hubert-Moy, L. Evaluation of Sentinel-1 & 2 time series for predicting wheat and rapeseed phenological stages. *ISPRS J. Photogramm. Remote Sens.* **2020**, *163*, 231–256.
- Steele-Dunne, S.C.; McNairn, H.; Monsivais-Huertero, A.; Judge, J.; Liu, P.-W.; Papathanassiou, K. Radar remote sensing of agricultural canopies: A review. *IEEE J. Sel. Top. Appl. Earth Obs. Remote Sens.* **2017**, *10*, 2249–2273. [[CrossRef](#)]
- Schlund, M.; Erasm, S. Sentinel-1 time series data for monitoring the phenology of winter wheat. *Remote Sens. Environ.* **2020**, *246*, 111814. [[CrossRef](#)]
- Harfenmeister, K.; Spengler, D.; Weltzien, C. Analyzing temporal and spatial characteristics of crop parameters using Sentinel-1 backscatter data. *Remote Sens.* **2019**, *11*, 1569. [[CrossRef](#)]
- Nasrallah, A.; Baghdadi, N.; El Hajj, M.; Darwish, T.; Belhouchette, H.; Faour, G.; Darwich, S.; Mhawe, M. Sentinel-1 data for winter wheat phenology monitoring and mapping. *Remote Sens.* **2019**, *11*, 2228. [[CrossRef](#)]
- McNairn, H.; Jiao, X.; Pacheco, A.; Sinha, A.; Tan, W.; Li, Y. Estimating canola phenology using synthetic aperture radar. *Remote Sens. Environ.* **2018**, *219*, 196–205. [[CrossRef](#)]
- Moreira, A.; Prats-Iraola, P.; Younis, M.; Krieger, G.; Hajnsek, I.; Papathanassiou, K.P. A tutorial on synthetic aperture radar. *IEEE Geosci. Remote Sens. Mag.* **2013**, *1*, 6–43. [[CrossRef](#)]
- Cloude, S.R.; Pottier, E. An entropy based classification scheme for land applications of polarimetric SAR. *IEEE Trans. Geosci. Remote Sens.* **1997**, *35*, 68–78. [[CrossRef](#)]
- Canisius, F.; Shang, J.; Liu, J.; Huang, X.; Ma, B.; Jiao, X.; Geng, X.; Kovacs, J.M.; Walters, D. Tracking crop phenological development using multi-temporal polarimetric Radarsat-2 data. *Remote Sens. Environ.* **2018**, *210*, 508–518. [[CrossRef](#)]
- He, Z.; Li, S.; Wang, Y.; Dai, L.; Lin, S. Monitoring Rice Phenology Based on Backscattering Characteristics of Multi-Temporal RADARSAT-2 Datasets. *Remote Sens.* **2018**, *10*, 340. [[CrossRef](#)]
- Mascolo, L.; Lopez-Sanchez, J.M.; Vicente-Guijalba, F.; Nunziata, F.; Migliaccio, M.; Mazzarella, G. A Complete Procedure for Crop Phenology Estimation with PolSAR Data Based on the Complex Wishart Classifier. *IEEE Trans. Geosci. Remote Sens.* **2016**, *54*, 6505–6515. [[CrossRef](#)]
- Wang, H.; Magagi, R.; Goita, K.; Trudel, M.; McNairn, H.; Powers, J. Crop phenology retrieval via polarimetric SAR decomposition and Random Forest algorithm. *Remote Sens. Environ.* **2019**, *231*, 111234. [[CrossRef](#)]
- Wang, H.; Magagi, R.; Goita, K. Polarimetric Decomposition for Monitoring Crop Growth Status. *IEEE Geosci. Remote Sens. Lett.* **2016**, *13*, 870–874. [[CrossRef](#)]
- Li, H.; Zhang, C.; Zhang, S.; Atkinson, P.M. Full year crop monitoring and separability assessment with fully-polarimetric L-band UAVSAR: A case study in the Sacramento Valley, California. *Int. J. Appl. Earth Obs. Geoinf.* **2019**, *74*, 45–56. [[CrossRef](#)]
- Lopez-Sanchez, J.M.; Vicente-Guijalba, F.; Ballester-Berman, J.D.; Cloude, S.R. Polarimetric response of rice fields at C-band: Analysis and phenology retrieval. *IEEE Trans. Geosci. Remote Sens.* **2013**, *52*, 2977–2993. [[CrossRef](#)]
- Vicente-Guijalba, F.; Martinez-Marin, T.; Lopez-Sanchez, J.M. Crop phenology estimation using a multitemporal model and a Kalman filtering strategy. *IEEE Geosci. Remote Sens. Lett.* **2013**, *11*, 1081–1085. [[CrossRef](#)]
- Küçük, Ç.; Taşkın, G.; Erten, E. Paddy-rice phenology classification based on machine-learning methods using multitemporal co-polar X-band SAR images. *IEEE J. Sel. Top. Appl. Earth Obs. Remote Sens.* **2016**, *9*, 2509–2519. [[CrossRef](#)]

29. Yang, Z.; Shao, Y.; Li, K.; Liu, Q.; Liu, L.; Brisco, B. An improved scheme for rice phenology estimation based on time-series multispectral HJ-1A/B and polarimetric RADARSAT-2 data. *Remote Sens. Environ.* **2017**, *195*, 184–201. [[CrossRef](#)]
30. Cloude, S. The dual polarization entropy/alpha decomposition: A PALSAR case study. *Sci. Appl. SAR Polarim. Polarim. Interferom.* **2007**, *644*, 2.
31. Ji, K.; Wu, Y. Scattering mechanism extraction by a modified Cloude-Pottier decomposition for dual polarization SAR. *Remote Sens.* **2015**, *7*, 7447–7470. [[CrossRef](#)]
32. Shan, Z.; Wang, C.; Zhang, H.; Chen, J. H-alpha decomposition and alternative parameters for dual Polarization SAR data. *PIERS Suzhou China* **2011**, *4*, 1386–1390.
33. Harfenmeister, K.; Itzerott, S.; Weltzien, C.; Spengler, D. Agricultural monitoring using polarimetric decomposition parameters of sentinel-1 data. *Remote Sens.* **2021**, *13*, 575. [[CrossRef](#)]
34. Dey, S.; Bhogapurapu, N.; Homayouni, S.; Bhattacharya, A.; McNairn, H. Unsupervised classification of crop growth stages with scattering parameters from dual-pol sentinel-1 SAR data. *Remote Sens.* **2021**, *13*, 4412. [[CrossRef](#)]
35. Harfenmeister, K.; Itzerott, S.; Weltzien, C.; Spengler, D. Detecting phenological development of winter wheat and winter barley using time series of sentinel-1 and sentinel-2. *Remote Sens.* **2021**, *13*, 5036. [[CrossRef](#)]
36. Haldar, D.; Verma, A.; Kumar, S.; Chauhan, P. Estimation of mustard and wheat phenology using multi-date Shannon entropy and Radar Vegetation Index from polarimetric Sentinel-1. *Geocarto Int.* **2022**, *37*, 5935–5962. [[CrossRef](#)]
37. Lopez-Sanchez, J.M.; Cloude, S.R.; Ballester-Berman, J.D. Rice phenology monitoring by means of SAR polarimetry at X-band. *IEEE Trans. Geosci. Remote Sens.* **2011**, *50*, 2695–2709. [[CrossRef](#)]
38. Pacheco, A.; McNairn, H.; Li, Y.; Lampropoulos, G.; Powers, J. Using RADARSAT-2 and TerraSAR-X satellite data for the identification of canola crop phenology. In *Remote Sensing for Agriculture, Ecosystems, and Hydrology XVIII*; SPIE: Edinburgh, UK, 2016; p. 999802.
39. Dong, J.; Fu, Y.; Wang, J.; Tian, H.; Fu, S.; Niu, Z.; Han, W.; Zheng, Y.; Huang, J.; Yuan, W. Early-season mapping of winter wheat in China based on Landsat and Sentinel images. *Earth Syst. Sci. Data* **2020**, *12*, 3081–3095. [[CrossRef](#)]
40. Cloude, S.R.; Goodenough, D.G.; Chen, H. Compact polarimetry for C-band land-use classification: A pre-study for the Canadian Radar Constellation Mission (RCM). In *Sar Image Analysis, Modeling, and Techniques XII*; SPIE: Edinburgh, UK, 2011; pp. 36–49.
41. Mascolo, L.; Lopez-Sanchez, J.M.; Cloude, S.R. Thermal noise removal from polarimetric Sentinel-1 data. *IEEE Geosci. Remote Sens. Lett.* **2021**, *19*, 1–5. [[CrossRef](#)]
42. Chauhan, S.; Darvishzadeh, R.; Boschetti, M.; Nelson, A. Discriminant analysis for lodging severity classification in wheat using RADARSAT-2 and Sentinel-1 data. *ISPRS J. Photogramm. Remote Sens.* **2020**, *164*, 138–151. [[CrossRef](#)]
43. Lee, J.-S.; Pottier, E. *Polarimetric Radar Imaging: From Basics to Applications*; CRC Press: Boca Raton, FL, USA, 2017.
44. Hajj, M.E.; Baghdadi, N.; Belaud, G.; Zribi, M.; Cheviron, B.; Courault, D.; Hagolle, O.; Charron, F. Irrigated grassland monitoring using a time series of terraSAR-X and COSMO-skyMed X-Band SAR Data. *Remote Sens.* **2014**, *6*, 10002–10032. [[CrossRef](#)]
45. Cookmartin, G.; Saich, P.; Quegan, S.; Cordey, R.; Burgess-Allen, P.; Sowter, A. Modeling microwave interactions with crops and comparison with ERS-2 SAR observations. *IEEE Trans. Geosci. Remote Sens.* **2000**, *38*, 658–670. [[CrossRef](#)]
46. Wang, H.; Magagi, R.; Goita, K. Potential of a two-component polarimetric decomposition at C-band for soil moisture retrieval over agricultural fields. *Remote Sens. Environ.* **2018**, *217*, 38–51. [[CrossRef](#)]
47. Fieuzal, R.; Baup, F.; Marais-Sicre, C. Monitoring wheat and rapeseed by using synchronous optical and radar satellite data—From temporal signatures to crop parameters estimation. *Adv. Remote Sens.* **2013**, *2*, 33222. [[CrossRef](#)]
48. Mattia, F.; Le Toan, T.; Picard, G.; Posa, F.I.; D’Alessio, A.; Notarnicola, C.; Gatti, A.M.; Rinaldi, M.; Satalino, G.; Pasquariello, G. Multitemporal C-band radar measurements on wheat fields. *IEEE Trans. Geosci. Remote Sens.* **2003**, *41*, 1551–1560. [[CrossRef](#)]
49. Balenzano, A.; Mattia, F.; Satalino, G.; Davidson, M.W. Dense temporal series of C-and L-band SAR data for soil moisture retrieval over agricultural crops. *IEEE J. Sel. Top. Appl. Earth Obs. Remote Sens.* **2010**, *4*, 439–450. [[CrossRef](#)]

Disclaimer/Publisher’s Note: The statements, opinions and data contained in all publications are solely those of the individual author(s) and contributor(s) and not of MDPI and/or the editor(s). MDPI and/or the editor(s) disclaim responsibility for any injury to people or property resulting from any ideas, methods, instructions or products referred to in the content.